VDMA
Fluid Power Association

22nd ISC

International Sealing Conference

Stuttgart, Germany
October 01 - 02, 2024

Sealing Technology –
Challenges accepted!

UNI STUTTGART

ISBN 978-3-8163-0768-6

Fachverband Fluidtechnik im VDMA e. V. Lyoner Str. 18
50628 Frankfurt am Main
Germany

Phone +49 69 6603-1513
E-Mail maximilian.baxmann@vdma.org
Internet www.vdma.org/fluid

Influence of surface topography on stick-slip-effects – an experimental and numerical study

Martin Wittmaack, Markus André, Sebastian Rakowski, Katharina Schmitz

Lubricated sealing systems tend to have undesirable stick-slip-effects under certain service conditions. This paper presents a tribometer test to analyze the influence of the surface topography on the stick-slip effect. In this test, it is possible to provoke or avoid the stick-slip effect by rotating the surface structure by 90°. Corresponding numerical contact- and CFD-simulations, based on the measured surface topography show clearly the influence of the surface structure on the flow in the lubrication gap. These numerical studies show the influence of the surface topography on the fluid dynamics in the lubrication gap of translational seals and enable a deeper understanding of the stick-slip mechanisms in lubricated sealing contacts.

1 Introduction

Lubricated sealing systems, such as in automotive brake master cylinders or other hydraulic systems, tend to have undesirable stick-slip-effects under certain service conditions. These stick-slip-effects are clearly driven by the complex frictional behavior in the mixed lubrication regime [1]. A significant factor in this tribological system is the surface topography. Thus, it is necessary to investigate and describe the lubrication effects on a micromechanical level. The systematic structuring of the surface topography can enhance the load carrying capacity of the lubricating film while simultaneously reducing friction [2, 3]. Furthermore, this targeted change in hydrodynamic lubrication allows minimizing the stick-slip tendency in pin on disk tribometer tests [4, 5].

In this paper, a tribometer test is presented and used to investigate the influence of surface structure on the stick-slip effect. Finally, numerical contact and CFD simulations are carried out based on measured surfaces, which show the influence of the surface topography on the flow in the lubrication gap and thus provide some conclusions on the complex friction behavior.

2 Tribometer test

The standard DIN 51834-5 [6], which is currently in the draft status, was recently published for the investigation of the stick-slip tendency of brake fluids in EPDM (ethylene propylene diene monomer rubber)-steel contacts. In this standard tribometer test, a roller bearing steel ball rubs on a roughened EPDM surface (point contact). This test procedure allows to successfully quantify the stick-slip tendency of brake fluids [7]. For a better tribological description of lubricated sealing systems, this standard test is modified so that an EPDM cord slides on a steel surface (line contact).

2.1 Experimental setup

In this test the tribometer presses a cylindrical $70\ \mathrm{ShA}$ EPDM specimen (Figure 1 - Item 2) (diameter: $5\ \mathrm{mm}$, length: $5\ \mathrm{mm}$) onto a ground C45 steel surface (Figure 1 - Item 4) with a defined normal force $F_N = 10, 20, 30\ \mathrm{N}$. The tribometer performs an oscillating motion $u(t)$ with the frequency $f = 1, \ldots, 6\ \mathrm{Hz}$ and an amplitude $a = 1.5\ mm$ according to

$$u(t) = a \cdot sin\,(2 \cdot \pi \cdot f \cdot t). \tag{1}$$

The specimen holder is connected to the tribometer with two flat springs with a thickness of $0.5\ \mathrm{mm}$. The resulting stiffness per spring is $315\ \mathrm{N/mm}$. The stiffness of the adapter can be adjusted using the flat springs. The fluid (Figure 1 - Item 3) to be tested covers the steel specimen. In this work, a brake fluid with a viscosity of $\eta = 11.5 \cdot 10^{-3}\ \mathrm{Pa \cdot s}$ and ethanol with a viscosity of $\eta = 1.2 \cdot 10^{-3}\ \mathrm{Pa \cdot s}$ are examined.

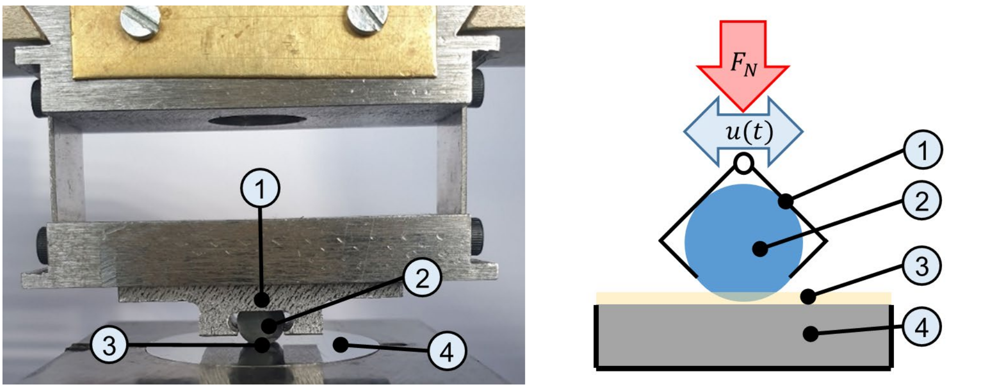

Figure 1: Experimental setup: 1) specimen holder; 2) cylindrical EPDM specimen; 3) fluid; 4) steel specimen

2.2 Investigated surfaces

The size of the analyzed surface section is $99.58 \times 99.58\ \mathrm{\mu m^2}$ and is measured with a confocal laser-scanning microscope (Keyence VK-100) with a resolution of $\Delta x = \Delta y = 0.341\ \mathrm{\mu m}$. This results in a surface resolution of 293×293 pixels. After the measurement, the curvature and the inclination of the measured surface are corrected using a second order polynomial. Furthermore, the measured data is smoothed with a 3x3 Gaussian matrix filter. Figure 2 shows the undeformed surfaces $r_{1,0}(x, y)$ and $r_{2,0}(x, y)$. As well, the visualization of the steel surface in Figure 2 as the roughness parameter in Table 1 and Table 2 show the clear anisotropic roughness of the steel surface due to grinding. The line roughness parameters are calculated for seven equidistant lines with an evaluation length of $89.349\ \mathrm{\mu m}$. The average values (Avg.) and the standard deviations (SD) of the multiple lines are listed in Table 1. Table 2 shows the surface roughness values for both surfaces.

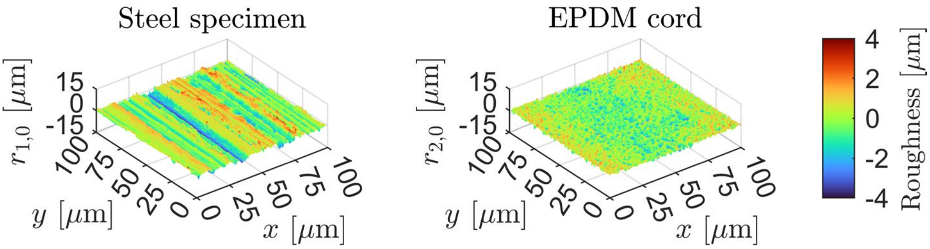

Figure 2: Examined surfaces

Table 1: Line roughness parameters of the examined surfaces

Surface	Direction		R_a [µm]	R_{pk} [µm]	R_k [µm]	R_{vk} [µm]	R_z [µm]
Steel	x	Avg.	0.964	0.911	2.748	1.522	6.605
		SD	0.038	0.314	0.195	0.191	0.509
Steel	y	Avg.	0.548	0.431	1.484	0.784	2.925
		SD	0.190	0.202	0.659	0.799	1.084
EPDM	x	Avg.	0.593	0.542	1.766	0.943	4.110
		SD	0.050	0.134	0.230	0.252	0.491
EPDM	y	Avg.	0.512	0.592	1.408	0.914	3.838
		SD	0.032	0.121	0.131	0.236	0.323

Table 2 Surface roughness parameters of the examined surfaces

Surface	S_a [µm]	S_{pk} [µm]	S_k [µm]	S_{vk} [µm]	S_{td} [°]	S_{tr} [−]
Steel	0.923	0.962	2.58	1.583	91.2	0.082
EPDM	0.649	0.671	1.972	1.081	82.8	0.132

2.3 Test results

Figure 3 shows the ratio of the friction force F_R to normal force F_N depending on the harmonic motion $u(t)$ for two orientations of the steel sample. In the load case shown, the normal force is $F_N = 20\ \mathrm{N}$ and the frequency $f = 4\ \mathrm{Hz}$. On the left side, the EPDM sample slides perpendicular ($\perp$) to the grinding direction. It can be seen, that no stick-slip effect occurs. The maximum ratio F_R/F_N occurs when the EPDM changes from sticking to sliding ($u \approx 1\ \mathrm{mm}, u \approx -1.2\ \mathrm{mm}$). Afterwards the friction force decreases and increases again as the sample slows down. However, if the steel sample is rotated by 90° so that the EPDM sample slides in the direction of grinding (right diagram (||)), the stick-slip effect occurs. In this case, the maximum ratio F_R/F_N during the change from sticking to sliding is nearly constant. The stick-slip effect is not only visible in the friction force signal, but is also clearly audible through squeaking noises.

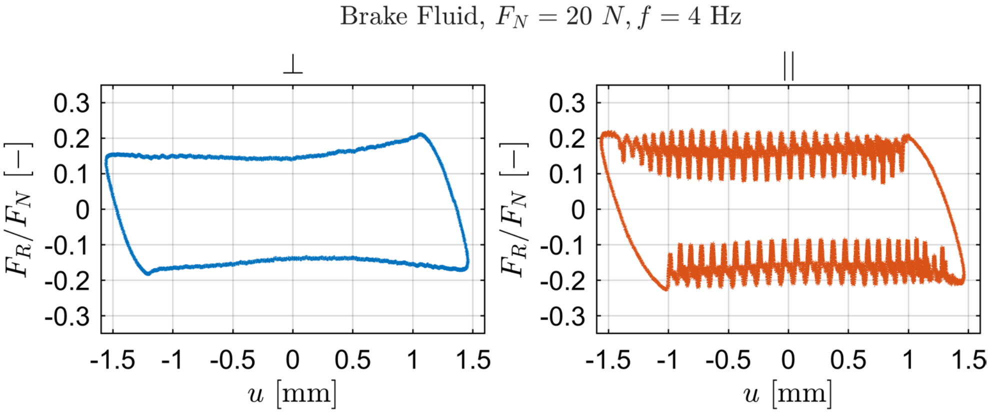

Figure 3: Measured ratio of friction force to normal force for two orientations of the steel sample for the brake fluid

For the quantification of the stick-slip tendency of a brake fluid to the standard DIN 51834-5 defines the stick-slip index σ. This index corresponds to the standard deviation of the oscillating force during stick-slip movement. Details on the calculation of the stick-slip index σ can be found in [6, 8].

Figure 4 shows the stick-slip index σ for the test program of the brake fluid. It is clearly visible, that no stick-slip occurs while the EPDM cord is rubbing perpendicular $\perp$ to the grinding direction. If the surface structure is orientated parallel to the moving direction, it can be seen that the stick-slip effect occurs with the exception of the frequency $f = 1$ Hz. The diagram shows also that the stick-slip index has a maximum at a frequency of $f = 4$ Hz and decreases again with higher excitation frequencies and the resulting higher sliding velocities.

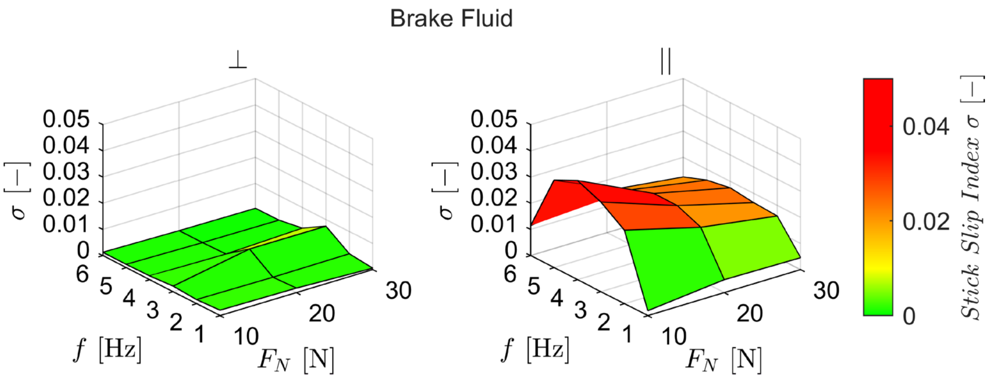

Figure 4: Stick-Slip Index force for two orientations of the steel sample for the brake fluid

Figure 5 shows the ratio of the friction force F_R to normal force F_N for the fluid Ethanol. Just as in the tests with brake fluid, the stick-slip effect occurs when sliding in the grinding direction (||) and does not occur when the EPDM cord is rubbing perpendicular (⊥) to the surface structure. Furthermore the friction force is higher compared to the brake fluid due to the lower lubricating effect of the ethanol.

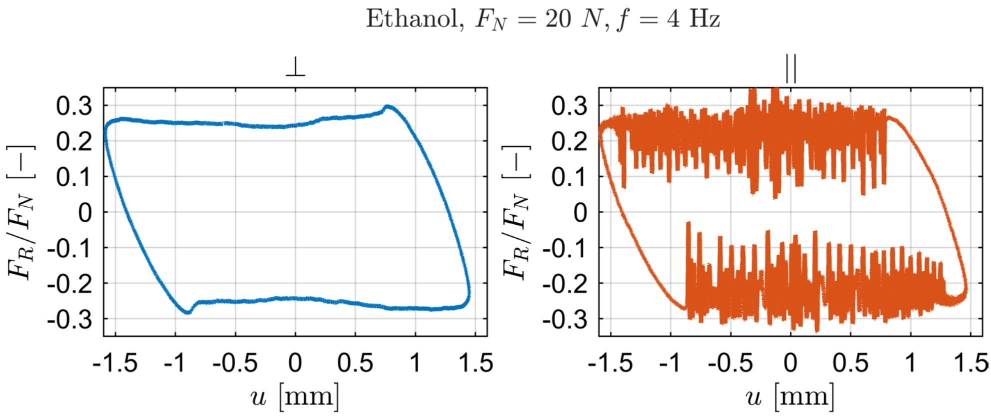

Figure 5: Measured ratio of friction force to normal force for two orientations of the steel sample for the fluid Ethanol

The stick-slip index for ethanol (Figure 6) also shows the dependence on the orientation of the surface structure. For movement perpendicular ⊥ to the grinding direction, there is no stick-slip effect. Similar to the brake fluid, no stick-slip occurs at a frequency of $f = 1\,\mathrm{Hz}$. According to the ratio F_R/F_N, the stick slip indexes σ are greater than for brake fluid due to the larger amplitudes. In addition, compared to the brake fluid, there is no drop in the index with increasing frequencies.

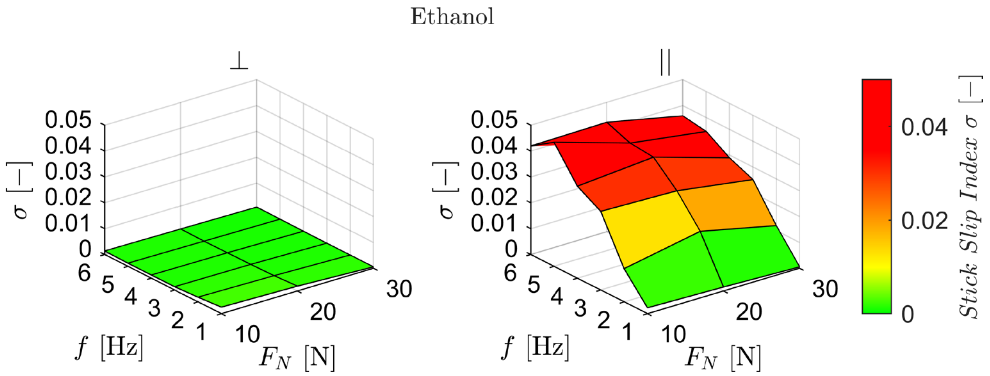

Figure 6: Stick-Slip Index force for two orientations of the steel sample for the fluid Ethanol

3 Numerical Study

For a deeper understanding of the test results, a numerical analysis of the tribological system is carried out below. For this purpose, the solid contact between the EPDM cord and the steel surface is first simulated on a microscopic scale. Subsequently, flow simulations between the deformed surfaces show the influence on the lubricating film.

3.1 Contact simulation on micro scale

Figure 7 shows the effective gap height $h(x,y)$, which is calculated from the difference between the z-coordinates of the deformed surfaces 1 and 2 to

$$h(x,y) = z_1(x,y) - z_2(x,y). \quad (2)$$

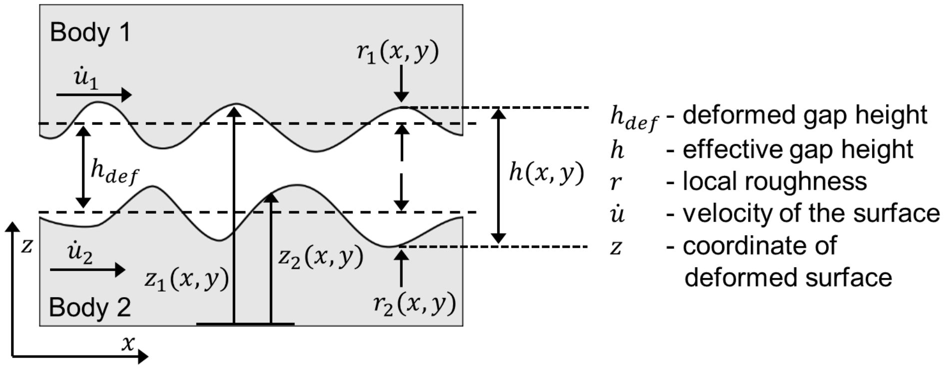

Figure 7: Definition of the gap height

In macroscopic component simulations, the surfaces of the parts are usually modelled as ideally smooth surfaces. This ideally smooth surface can be interpreted as the average plane of roughness. In this sense, the deformed gap height h_{def} takes into account the mechanical deformations caused by the local contact of the two surfaces. It is calculated by averaging over the examined surface section Ω as follows

$$h_{def} = \frac{1}{\Omega} \int_{(\Omega)} h(x,y)\, d\Omega. \quad (3)$$

To describe the elastic deformations in the solid contact and the normal force as a function of the distance between the two rough surfaces, a contact simulation of real measured surfaces (Figure 2) is carried out on a microscopic scale. An elastic half-space model is used for this purpose, by solving the Boussinesq equation according to Bartel [9].

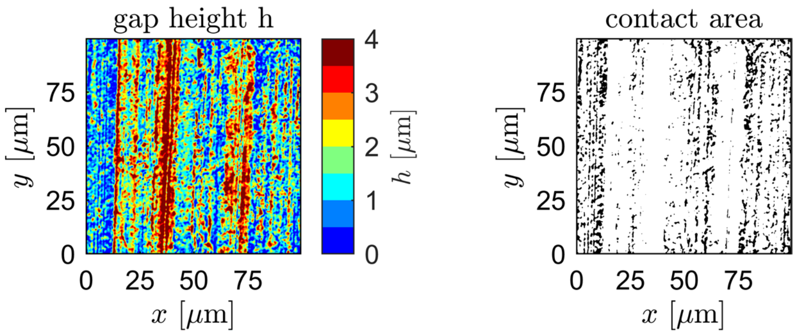

Figure 8: Gap height $h(x,y)$ and the real contact area at $h_{def} = 2.06\ \mu m$

Figure 8 shows on the left side an example of the effective gap height $h(x,y)$ at the deformed gap height $h_{def} = 2.06\ \mu\text{m}$. The structure of the steel surface is still clearly visible. In addition to the effective gap height $h(x,y)$, Figure 8 shows the real contact area. It can be seen that contact only occurs at the roughness peaks of the steel surface.

3.2 Flow simulation

The common approach to describe the lubricant film is the Reynolds equation. Assuming an incompressible Newtonian fluid (density $\rho = \text{const.}$, viscosity $\eta = \text{const.}$), this equation depends on the gap height h, the pressure gradients $\partial p/\partial x$ and $\partial p/\partial y$, the tangential velocities $\dot{u}$ and $\dot{v}$ of the moving surfaces 1 and 2

$$\frac{\partial}{\partial x}\left(\frac{h^3}{12\eta}\frac{\partial p}{\partial x}\right) + \frac{\partial}{\partial y}\left(\frac{h^3}{12\eta}\frac{\partial p}{\partial y}\right) = \frac{\dot{u}_1 + \dot{u}_2}{2}\frac{\partial h}{\partial x} + \frac{\dot{v}_1 + \dot{v}_2}{2}\frac{\partial h}{\partial y}. \tag{4}$$

The components of the specific volume flows q for the x- and y-direction are computed as follow

$$q_x = \frac{h^3}{12 \cdot \eta}\frac{\partial p}{\partial x} - \frac{\dot{u}_1 + \dot{u}_2}{2}h$$

and (5)

$$q_y = \frac{h^3}{12 \cdot \eta}\frac{\partial p}{\partial y} - \frac{\dot{v}_1 + \dot{v}_2}{2}h.$$

The specific volume flow can be determined from the directional components (Equation (4))

$$q = \sqrt{q_x^2 + q_y^2}. \tag{6}$$

To perform a computational fluid dynamic (CFD) simulation of the lubrication film, the Reynolds equation (4) is used and is solved by applying the finite difference method (FDM). The FDM uses a central difference scheme according to Equation (7). The derivations in the y-direction are computed accordingly. This FDM scheme is implemented in the mathematics program MATLAB.

$$\left(\frac{\partial p}{\partial x}\right)_{j,i} = \frac{p_{j,i+1} - p_{j,i-1}}{2 \cdot \Delta x}$$
$$\left(\frac{\partial^2 p}{\partial x^2}\right)_{j,i} = \frac{p_{j,i+1} - 2 \cdot p_{j,i} + p_{j,i-1}}{\Delta x^2} \tag{7}$$

The previously performed contact simulation using a half-space model provides the deformed gap geometries $h(x, y)$ for several deformed gap heights h_{def}. These deformed gap geometries are now used to perform both pressure and shear flow simulations for the brake fluid ($\eta = 11.5 \cdot 10^{-3}\ \mathrm{Pa \cdot s}$). In order to obtain a more accurate solution the mesh is refined using a cubic spline. In the pressure flow simulation, 10 additional points are generated between the individual pixels. For the shear flow simulation 20 additional points are generated between the individual pixels.

3.2.1 Results of the flow simulation

To carry out the pressure flow simulation, a fluid pressure of $p_{in} = 0.2\ \mathrm{MPa}$ is specified on the inlet side $(x = 0)$ and a fluid pressure of $p_{out} = 0.1\ \mathrm{MPa}$ on the outlet side($x = 99.58\ \mathrm{\mu m}$). The surface velocities are assumed to be zero ($\dot{u}_1 = \dot{u}_2 = \dot{v}_1 = \dot{v}_2 = 0$). The flow of the fluid is prevented by specifying a pressure gradient $(\partial p/\partial y)$ equal to zero on the sides($y = 0, y = 99.58\ \mathrm{\mu m}$). Figure 9 shows the specific volume flow for the pressure flow simulation at a deformed gap height of $h_{def} = 2.06\ \mathrm{\mu m}$. If the fluid flows perpendicular (⊥) to the grinding direction, the roughness impedes the fluid. The fluid therefore flows through branched channels. If the fluid flows in grinding direction (||), the surface topography supports the fluid flow, which results in a higher specific volume flow.

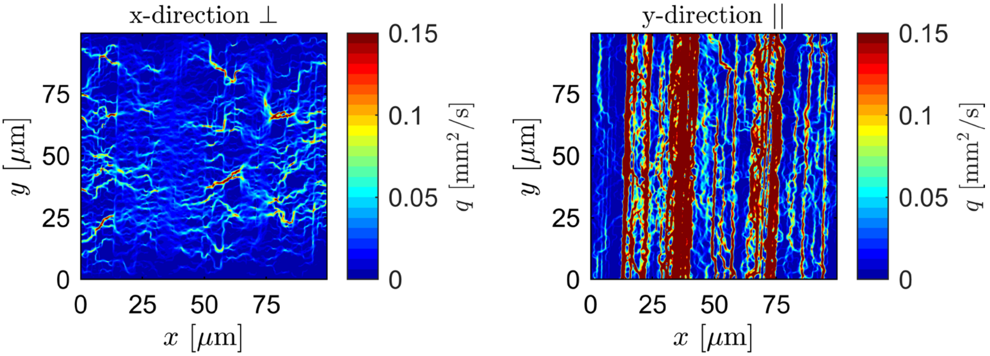

Figure 9: Specific volume flow for the pressure flow simulation at $h_{def} = 2.06\ \mu m$

For the shear flow simulation, the same pressure is defined on the inlet and outlet side $p_{in} = p_{out}$. The velocities of the surfaces are specified in opposite directions to each other in the direction of flow ($\dot{u}_1 = -\dot{u}_2 = 100\ \mathrm{mm/s}$). Similar to the pressure flow simulation, a pressure gradient equal to zero prevents the fluid from flowing out over the sides. Figure 10 shows the specific volume flow for this load case at a deformed gap height $h_{def} = 2.06\ \mathrm{\mu m}$. If the surfaces move perpendicular (⊥) to the grinding direction, the roughness valleys transport more fluid than if they move parallel (||) to the surface structure.

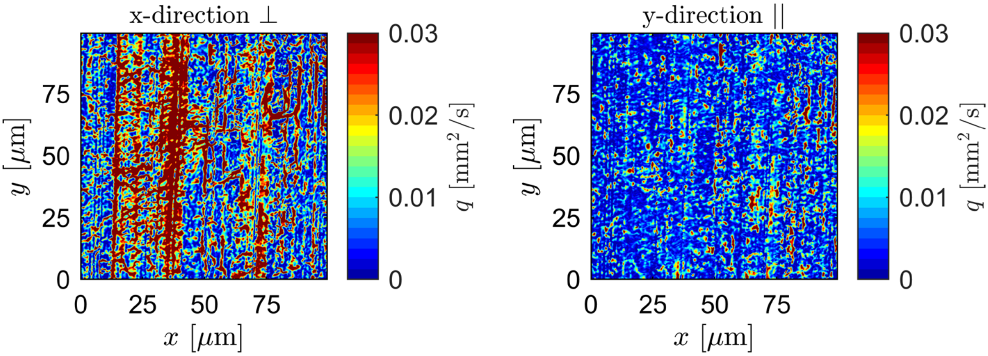

Figure 10: Specific volume flow for the shear flow simulation at $h_{def} = 2.06\ \mu m$

If the EPDM cord rubs perpendicular to the grinding direction, the surface topography hinders the fluid so it enters the lubrication gap. At the same time, the surface topography in the lubrication gap impedes the volume flow and thus supports the build-up of fluid pressure. If the EPDM cord now switches between sticking and slipping, a lubricating film builds up. Once this has built up, the surface topography prevents the fluid from flowing out, resulting in a stable lubricating film. However, if the EPDM cord rubs in the direction of grinding (||), the cord partially pushes the fluid in front of it. Within the lubrication gap, the surface topography supports the volume flow. When alternating between sliding and sticking, a smaller lubricating film builds up compared to the perpendicular movement. Furthermore, the surface structure allows the fluid to flow off again quickly. This is why the contact quickly switches back from slipping to sticking.

3.2.2 Flow Factors

Usually the Reynolds equation (4) above describes the fluid film dynamics for smooth surfaces. The direct depiction of surface roughness in component simulation would be associated with a large computational effort due to the differences in scale (component simulation $[\mathrm{mm}]$ – surface topography $[\mu\mathrm{m}]$). Therefore, the method of flow factors by Patir and Cheng [10, 11] is often used to describe the influence of roughness on the flow in the lubrication gap. For further illustration of this roughness influence, the flow factors are calculated below based on the previous flow simulations.

The flow factor method extends the Reynolds equation (4) by the pressure flow factor Φ^{p} and the shear flow factor Φ^{s}. The pressure flow factor Φ^{p} scales the Poiseuille term of the Reynolds equation and describes the influence of the surface roughness on the fluid film. Additional Couette terms containing the shear flow factors Φ^{s} describe the additional fluid transport through the surface roughness. By adding the flow factors, the Reynolds equation is obtained as follows

$$\frac{\partial}{\partial x}\left(\Phi_x^p \cdot \frac{h^3}{12\cdot\eta}\frac{\partial p}{\partial x}\right) + \frac{\partial}{\partial y}\left(\Phi_y^p \cdot \frac{h^3}{12\cdot\eta}\frac{\partial p}{\partial y}\right) =$$
$$\frac{\partial}{\partial x}\left(\frac{\dot{u}_1+\dot{u}_2}{2}h + \frac{\dot{u}_1-\dot{u}_2}{2}\Phi_x^s\right) + \frac{\partial}{\partial y}\left(\frac{\dot{v}_1+\dot{v}_2}{2}h + \frac{\dot{v}_1-\dot{v}_2}{2}\Phi_y^s\right). \tag{8}$$

The pressure flow factor Φ^{p} (Equation (9)) indicates the ratio of the average specific volume flows of the pressure flow in the rough gap $\bar{q}_{rough}$ and the pressure flow in the ideally smooth gap $\bar{q}_{smooth}$. The average volume flow is calculated from the integration over the examined surface section Ω.

$$\Phi_x^{\mathrm{p}} = \frac{\bar{q}_{rough,x}}{\bar{q}_{smooth,y}} = \frac{1}{h_{def}^3 \cdot \frac{p_{in}-p_{out}}{L_x}} \cdot \left(\frac{1}{\Omega}\int_{(A)} \frac{h^3}{12\cdot\eta}\frac{\partial p}{\partial x}\, d\Omega\right) \tag{9}$$

Based on the shear flow simulation carried out above, the shear flow factor Φ^{s} is calculated from the average specific volume flow and velocities of the surfaces as follows

$$\Phi^{\mathrm{s}} = \frac{2}{\dot{u}_1-\dot{u}_2} \cdot \left(\frac{1}{\Omega}\int_{(A)} \frac{h^3}{12\cdot\eta}\frac{\partial p}{\partial x}\, d\Omega\right). \tag{10}$$

Figure 11 shows the pressure and shear flow factors depending on the sliding direction. A dashed line marks the deformed gap height h_{def} of the pressure flow simulation in Figure 9. In the pressure flow simulation perpendicular ($\perp$) to the surface structure, the specific volume flow is smaller than for a flow between two smooth surfaces, which results in $\Phi^p < 1$. At the marked deformed gap height $h_{def} = 2.06\ \mu m$, flow is barley possible because there is almost solid contact at the peaks of the roughness, which can also be seen from the contact area shown in Figure 8. The pressure flow simulation parallel (||) to the roughness results in $\Phi^p > 1$, because the surface topography favors the fluid. It is noticeable here that Φ^p drops again for small gap widths. The reason for this is that the individual flow channels are blocked by the solid contact as the gap becomes smaller. This behavior correlates very well with the specific volume flows of the pressure flow simulation, shown in Figure 9.

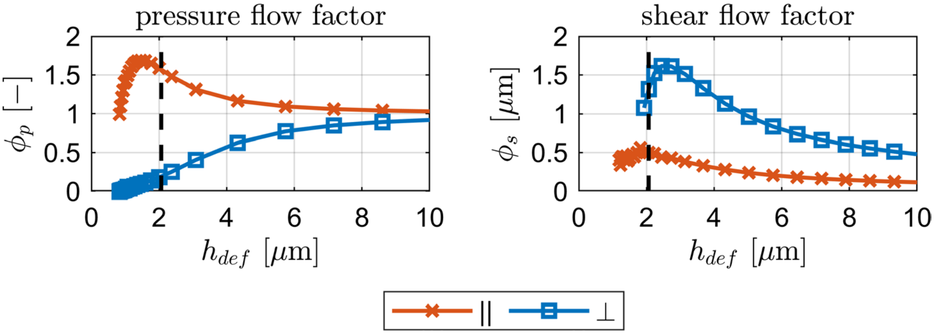

Figure 11: Flow factors for the flow parallel || and perpendicular ⊥ to grinding direction

The comparison of the shear flow factors Φ^s shows that more fluid is transported in the flow perpendicular to the surface structure. The shear flow factor reaches its maximum for the flow perpendicular to the roughness at $h_{def} = 3\ \mu\text{m}$ and then declines again due to the increasing solid contacts.

4 Summary and Conclusion

To investigate the influence of surface topography on stick-slip effects, a standard tribometer test was improved in order to better represent the tribological system of a lubricated dynamic seal. In addition to quantifying the stick-slip tendency of individual fluids, this test also enables the investigation of the influence of the surface structure on stick-slip effects. By rotating the surface structure, it is possible to provoke and prevent the stick-slip effect.

Furthermore, contact and CFD simulations based on measured surfaces are carried out to check the plausibility of the results. These simulations clearly show the influence of the surface topography on the lubricating film. If the EPDM cord slides perpendicular to the grinding direction, the flow is prevented through the surface structure, which favors the buildup of a stable fluid film, which results in no stick-slip effect. If the EPDM cord slides parallel to the grinding direction, the surface structure favors the flow, so that the fluid can quickly flow out again during sticking and the lubricating film that has formed collapses, which supports the occurrence of stick-slip effects.

By combining experiment and simulation, this work contributes to a deeper understanding of stick-slip effects and the influence of surface structuring on them.

5 Acknowledgements

We thank FREUDENBERG Sealing Technologies for providing the EPDM cords.

6 Nomenclature

Variable	***Description***	***Unit***
a	Amplitude	[mm]
f	Frequency of the tribometer	[Hz]
F_N	Normal Force	[N]
F_R	Friction Force	[N]
h	Effective Gap Height	[µm]
h_{def}	Deformed Gap Height	[µm]
p	Pressure	[MPa]
q	Specific Volume Flow	[mm²/s]

$\bar{q}$	Average Specific Volume Flow	[mm²/s]
r	Local Roughness	[µm]
u	Displacement in x –direction	[mm]
$\dot{u}$	Velocity in x –direction	[mm/s]
$\dot{v}$	Velocity in y –direction	[mm/s]
x	Coordinate	[mm]
y	Coordinate	[mm]
z	Coordinate	[mm]
η	Viscosity	[Pa·s]
Φ^p	Pressure Flow Factor	[-]
Φ^s	Shear Flow Factor	[µm]
ρ	Density	[g/cm³]
σ	Stick-Slip Index	[-]
Ω	Surface section	[mm²]

7 References

[1] Ibrahim, R. A.: *Friction-Induced Vibration, Chatter, Squeal, and Chaos—Part I: Mechanics of Contact and Friction*, In: Applied Mechanics Reviews, Vol. 47-7/1994, pp. 209-226,1994, https://doi.org/10.1115/1.3111079

[2] Etison, I., Burstein, L.: A Model for Mechanical Seals with Regular Microsurface Structure, In: Tribology Transactions, Vol 39-3/1996, pp. 677-683, 1996, https://doi.org/10.1080/10402009608983582

[3] Keller, D., Jacobs, G., Neumann, S.: *Development of a Low-Friction Radial Shaft Seal: Using CFD Simulations to Optimise the Microstructured Sealing Lip*, In: Lubricants, Vol 8-4/2020, 41, 2020, https://doi.org/10.3390/lubricants8040041

[4] Wang, H., Xie, X., Hua, X., Yin, B., Du, H., Xu, S., Qiu, B. J.: *The effect of laser surface texturing to inhibit stick-slip phenomenon in sliding contact*, In: Advances in Mechanical Engineering, Vol. 11-9/2019, pp. 1-10, 2019, https://doi.org/10.1177/1687814019874635

[5] He, Y., Yang, J., Wang, H., Gu, Z., Fu, Y.: *Micro-dimple and micro-bulge textures:Influence of surface topography types on stick–slip behavior under starved lubrication*, In: Applied Surface Science, Vol. 585, 2022, https://doi.org/10.1016/j.apsusc.2022.152501

[6] E DIN 51834-5:2022-10: *Prüfung von Schmierstoffen - Tribologische Prüfung im translatorischen Oszillations-Prüfgerät - Teil 5: Quantifizierung der reibungsbedingten Geräuschentwicklung von Bremsflüssigkeiten in EPDM-Stahl-Kontakten*, Beuth-Verlag, Berlin, 2022

[7] Wittmaack, M, André, M., Schmitz, K.: *Dynamic Friction Model for the Investigation of Stick-Slip Oscillations*, In: Chemical Engineering and Technology, Vol. 46-1/2023, pp. 28-36, 2023, https://doi.org/10.1002/ceat.202200416

[8] Wittmaack, M., André, M., Molter, J.: *Analyse von Einflussparametern auf den Stick-Slip Effekt mittels Tribometerversuchen und FE-Simulation.* In: Tribologie und Schmierungstechnik, Vol 69-1/2022, pp. 5-14; 2022, https://doi.org/10.24053/TuS-2022-0002

[9] Bartel, D.: *Simulation von Tribosystemen. Grundlagen und Anwendungen*, Vieweg + Teubner, Wiesbaden, 2010

[10] Patir, N., Cheng, H. S.: *An Average Flow Model for Determining Effects of Three-Dimensional Roughness on Partial Hydrodynamic Lubrication*, In: Journal of Lubrication Technology, Vol 100-1/1978, pp. 12-17, 1978, https://doi.org/10.1115/1.3453103

[11] Patir, N. u. Cheng, H. S.: *Application of Average Flow Model to Lubrication Between Rough Sliding Surfaces*, In: Journal of Lubrication Technology, Vol 101-2/1979, pp. 220-229, 1979, https://doi.org/10.1115/1.3453329

8 Authors

Hochschule Hannover, University of Applied Sciences and Arts Hannover, Faculty II – Mechanical and Bioprocess Engineering

Ricklinger Stadtweg 120, 30459 Hannover, Germany:

Martin Wittmaack, M. Eng., ORCID 0000-0003-3879-0274, Martin.Wittmaack@hs-hannover.de

Prof. Dr.-Ing. Markus André, Markus.Andre@hs-hannover.de

Prof. Dr.-Ing. Sebastian Rakowski, ORCID 0009-0004-5197-4398, Sebastian.Rakowski@hs-hannover.de

RWTH Aachen University, Institute for Fluid Power Drives and Systems (ifas)

Campus-Boulevard 30, 52074 Aachen, Germany:

Univ.-Prof. Dr.-Ing. Katharina Schmitz, ORCID 0000-0002-1454-8267, Katharina.Schmitz@ifas.rwth-aachen.de

https://doi.org/10.61319/YPUC46M7